Supplementary Information for

Topographic De-adhesion in the Viscoelastic Limit

Nhung Nguyen, Eugenio Hamm Hahn, Sachin Velankar, Enrique Cerda and Luka Pocivavsek*

* **Corresponding author. E-mail: lpocivavsek@bsd.uchicago.edu**

This PDF file includes:

Supplementary text
Figs. S1 to S5
Legend for Movie S1
SI References

Other supplementary materials for this manuscript include the following:

Movie S1

Supporting Information Text

Appendix 1: Mechanical analog and energy components for a viscoelastic solid

Consider a viscoelastic Maxwell solid shown in Figure S1. By considering either a displacement controlled experiment or a force controlled experiment applied to this system, it is straightforward to see that this system yields the right behavior as the viscoelastic model with a single Prony series: $E(t) = E_\infty + (E_0 - E_\infty)e^{-t/\tau_R}$ used in the main text. In order to physically understand different energy components in a viscoelastic system, a mass is added to the end of this system to include inertial effects. By applying a force F to the mass, the following equation of motion is obtained:

$$m\ddot{x} = -E_\infty x - (E_0 - E_\infty)x_1 + F, \quad [1]$$

where x is the total displacement of the system and x_1 is the displacement of the spring with stiffness $E_0 - E_\infty$. The dashpot is always in equilibrium with the contiguous spring and follows the equilibrium equation

$$\eta\dot{x_2} = (E_0 - E_\infty)x_1, \quad [2]$$

where $x_2 = x - x_1$ corresponds to the dashpot displacement. It defines the relaxation time $\tau_R = \eta/(E_0 - E_\infty)$ that accounts for different response regimes of the system. For quasi-static motion or zero inertial effects ($m\ddot{x} = 0$), the applied force is in balance with the springs and dashpot $F = E_\infty x + (E_0 - E_\infty)x_1$. For short times, $t \ll \tau_R$, the dashpot does not have sufficient time to react and $x_2 \approx 0$. It yields the force-displacement relation $F = E_0 x$. For large times, $t \gg \tau_R$, the dashpot has time to relax and $x_2 \approx x$. It means that the spring with stiffness E_∞ takes the total load applied to the system and $F = E_\infty x$. In general, the force-displacement relation is

$$F(t) = E_0 x(t) + \int_0^t d\tau x(\tau)\frac{d}{dt}E(t-\tau), \quad [3]$$

where $E(t) = E_\infty + (E_0 - E_\infty)e^{-t/\tau_R}$.

The energy balance is obtained by multiplying Equation 1 by $\dot{x}$ and integrating by parts:

$$\frac{d}{dt}\left[\frac{m}{2}\dot{x}^2 + \frac{E_\infty}{2}x^2 + \frac{E_0 - E_\infty}{2}x_1^2\right] = -\eta\dot{x_2}^2 + F\dot{x}. \quad [4]$$

Here, we recognize the kinetic energy T, the stored energy U, and the total energy $E = T + U$, which can be defined as:

$$\begin{aligned} E &= T + U, \\ T &= \frac{m}{2}\dot{x}^2, \\ U &= \frac{E_\infty}{2}\dot{x}^2 + \frac{E_0 - E_\infty}{2}\dot{x_1}^2. \end{aligned} \quad [5]$$

This leads to

$$\frac{dE}{dt} = -\eta\dot{x_2}^2 + F\dot{x}, \quad [6]$$

from which the rate of dissipation can be recognized as $\dot{D} = \eta\dot{x_2}^2$ and the external work per unit of time $\dot{W} = F\dot{x}$. In other words,

$$\frac{dE}{dt} = -\dot{D} + \dot{W}. \quad [7]$$

This states that the total mechanical energy decreases by dissipation and increases by the external work applied to the system(1). Thus, by using the mechanical analog above, a physical view of different energy components is elucidated and the stored energy is the elastic energy of the two springs. The analysis can also be generalized to a continuum system. Consider the case of uniaxial compression, traction, or bending of a filament where we expect the following constitutive relation:

$$\sigma = E_\infty\epsilon + (E_0 - E_\infty)\epsilon^e. \quad [8]$$

Here ϵ^e is not the complete strain ϵ because part of the strain is taken by a viscous term ϵ^v such that $\epsilon = \epsilon^e + \epsilon^v$. In this regard, ϵ^e and ϵ^v are equivalent to x_1 and x_2, respectively, in the previous model. With no viscous term, the effective stiffness of the system is E_0, however, the viscous term dissipates the elasticity of the contiguous spring with stiffness $E_0 - E_\infty$ and the effective stiffness for long times is E_∞. The stress of the spring with stiffness $E_0 - E_\infty$ is in balance with a viscous stress: $\sigma^e = \sigma^v$. It yields:

$$(E_0 - E_\infty)\epsilon^e = 2\eta\dot{\epsilon}^v, \quad [9]$$

where we use the constitutive relation $\sigma^v = 2\eta\dot{\epsilon}$ to describe the uniaxial deformation of a viscous fluid. Thus, the following representation for the viscous strain in terms of the total strain is obtained:

$$2\eta\dot{\epsilon}^v = (E_0 - E_\infty)(\epsilon - \epsilon^v). \quad [10]$$

Defining the relaxation time $\tau_R = 2\eta/(E_0 - E_\infty)$, we obtain the equation:

$$\tau_R \dot{\epsilon}^v = \epsilon - \epsilon^v, \quad [11]$$

that allows us to find the viscous strain:

$$\epsilon^v = \frac{1}{\tau_R}\int_0^t \epsilon(\tau) e^{-(t-\tau)/\tau_R} d\tau. \quad [12]$$

Thus, the stored energy as the elastic energy of the two springs is generalized as:

$$U = \frac{E_\infty}{2}\int_V dV \epsilon^2 + \frac{E_0 - E_\infty}{2}\int_V dV \left(\epsilon^e\right)^2. \quad [13]$$

The above relation corresponds to the one presented by Christensen(1) where the stored energy is computed as:

$$U = \frac{1}{2}\int_{-\infty}^t \int_{-\infty}^t E(2t - \tau - \zeta)\frac{d\epsilon}{d\tau}\frac{d\epsilon}{d\zeta} d\epsilon d\zeta. \quad [14]$$

The total energy of the viscoelastic solid corresponds to the total injected work to the system, which is:

$$\dot{W} = \int_V \sigma \dot{\epsilon} dV. \quad [15]$$

Appendix 2: Analytical method for wrinkle induced delamination

From the imposed wrinkled topography $h(x,t) = A(t)\sin(kx)$, the imposed strain in the foulant layer is:

$$\gamma = -yk^2 A(t)\sin(kx), \quad [16]$$

where $A(t) = \frac{2}{k}\sqrt{\dot{\epsilon}(t - t_w)}$. Neglecting the part of the strain previous to buckling and taking $t_w = 0$, the viscous strain is computed as:

$$\gamma^v = yk^2 \frac{2}{k}\sin(kx)\sqrt{\dot{\epsilon}\tau_R} F(t/\tau_R), \quad [17]$$

where $F(x) = \int_0^x \sqrt{y} e^{-(x-y)} dy$. Therefore, the elastic strain is:

$$\gamma^e = yk^2 \sin(kx)\left[A(t) - A(\tau_R)F(t/\tau_R)\right]. \quad [18]$$

Here $A(t) = \frac{2}{k}\sqrt{\dot{\epsilon}t}$ because of the approximations. We can now compute the stored energy and the total work. The stored energy should be the elastic energy of the two springs (Equation 13, Appendix 1) which becomes:

$$U/L = \frac{E_\infty I}{4}\left[k^2 A(t)\right]^2 + \frac{(E_0 - E_\infty)I}{4}\left[k^2(A(t) - A(\tau_R)F(t/\tau_R))\right]^2. \quad [19]$$

The total work in Equation 15 of Appendix 1 becomes:

$$W/L = \frac{E_0 I}{4}\left[k^2 A(t)\right]^2 - \frac{(E_0 - E_\infty)I}{4}\left[k^2 A(\tau_R)\right]^2 H(\tau/\tau_R), \quad [20]$$

where $H(z)$ is a dimensionless integral, so that

$$H(z) = \int_0^z dw \frac{F(w)}{\sqrt{w}} = zP_-(z), \quad [21]$$

$$P_-(z) = 1 - {}_2F_2[1,1;\frac{3}{2},2;-z]. \quad [22]$$

Note that ${}_2F_2[1,1;\frac{3}{2},2;-z]$ is a hypergeometric function of order $(2,2)$.

To drive the fracture in a viscoelastic system, approaches balancing either the total work or the stored energy against the fracture toughness have been proposed in the literature(2, 3). We first start with the consideration of the balance using the total work: $0 = d(W + U_S)$, where the surface energy is $U_S = Gbl$, where G is the work of fracture, b is the film width, l is the crack length. This leads to:

$$\frac{B_0}{4}\left[k^2 A(t)\right]^2 - \frac{B_0 - B_\infty}{4}\left[k^2 A(\tau_R)\right]^2 H(t/\tau_R) = G. \quad [23]$$

Using the relation $H(z) = zP_-(z)$, this can be rewritten:

$$\frac{B_0}{4}\left[k^2 A(t)\right]^2 - \frac{B_0 - B_\infty}{4}\left[k^2 A(t)\right]^2 P_-(t/\tau_R) = G. \quad [24]$$

Therefore,

$$t_c/\tau_R \sim \frac{\lambda^2 G/(B_0 \dot{\epsilon} \tau_R)}{[1-\beta P_-(t_c/\tau_R)]}. \quad [25]$$

For the energy balance approach using the stored energy: $0 = d(U + U_S)$, the following relation is obtained:

$$\frac{B_\infty}{4}\left[k^2 A(t)\right]^2 + \frac{B_0 - B_\infty}{4}\left[k^2\left(A(t) - A(\tau_R)F(t/\tau_R)\right)\right]^2 = G. \quad [26]$$

Defining the function $P_+(z) = \left[1 - \left(1 - \frac{F(z)}{\sqrt{z}}\right)^2\right]$, this relation is rewritten as follows:

$$\frac{B_0}{4}\left[k^2 A(t)\right]^2 - \frac{B_0 - B_\infty}{4}\left[k^2 A(t)\right]^2 P_+(t/\tau_R) = G. \quad [27]$$

Therefore,

$$t_c/\tau_R \sim \frac{\lambda^2 G/(B_0 \dot{\epsilon} \tau_R)}{[1-\beta P_+(t_c/\tau_R)]}. \quad [28]$$

Thus, the non-linear equations to determine the critical delamination time for both approaches have the same following forms:

$$t_c/\tau_R \sim \frac{\lambda^2 G/(B_0 \dot{\epsilon} \tau_R)}{[1-\beta P_\pm(t_c/\tau_R)]}, \quad [29]$$

with P_+ and P_- defined above. Note that these two functions are bounded between 0 and 1, and $P_+(z) > P_-(z)$. We observe the followings:
For $\lambda^2 G/(B_0 \dot{\epsilon} \tau_R) \ll 1$ and $\beta \ll 1$, then

$$t_c/\tau_R \sim \lambda^2 G/(B_0 \dot{\epsilon} \tau_R). \quad [30]$$

For $\lambda^2 G/(B_0 \dot{\epsilon} \tau_R) \gg 1$, then

$$t_c/\tau_R \sim \frac{\lambda^2 G/(B_0 \dot{\epsilon} \tau_R)}{1-\beta}. \quad [31]$$

The above non-linear equations are solved in MATLAB (Mathworks, MA) for varying combinations of dimensionless parameters and results are shown in Figure S3b of the main text.

Appendix 3: Numerical modeling with finite element (FE) and cohesive zone method (CZM)

Details of the FE model using Abaqus Explicit for the tri-layer system (foulant layer, film, and substrate) with the specified boundary conditions in the main manuscript are provided in the previous study(4). Each layer is modeled with three-dimensional solid elements (C3D8R, 8-node linear brick, reduced integration, and with hourglass control). The front and back faces are constrained in the z direction to maintain an effective plane strain condition. The foulant layer is described by the linear viscoelastic constitutive relationship with a single Prony series: $E(t) = E_\infty + (E_0 - E_\infty)e^{-t/\tau_R}$ while the film and the substrate are modeled as incompressible, neo-Hookean materials. The modulus of the foulant layer $E_p(t)$ is much smaller than the modulus of the film E_f such that $B_p \ll B_f$. The ratio between the moduli of the film and the substrate is $E_f/E_s \sim 80$. In order to model delamination of the foulant layer, the interface between the foulant layer and the film is modeled using Abaqus cohesive interface(5) with bi-linear traction separation laws as shown in Figure S2. This bi-linear shape for the traction separation law reduced numerical singularity caused by the abrupt drop of stress in the right-triangular traction profile used in the previous study(4).

Though mixed-mode delamination(6, 7) can be important along this wrinkled interface, to simplify the problem, here independent traction separation laws as shown in Figure S2 for the normal and tangential modes are used in this study. In addition, due to the lack of experimental data for the critical strength σ_c, τ_c and fracture toughness G_{IC}, G_{IIC} for the biologically relevant interfaces considered here, $\sigma_c = \tau_c$ and $G_{IC} = G_{IIC} = G$ are assumed for the traction separation laws*. Note that delamination only occurs when at least one CZM element on the interface reaches the end of the traction separation law. In other words, the stress must reach the critical value and the energy must be dissipated by an amount equal to G so that the fracture surface can be created. Hence, both stress and energy are used as criteria for fracture onset as well as propagation in CZM. The delamination onset is followed by checking the CSDMG parameter in Abaqus, which reaches the value of 1 when the traction reaches the end of the traction separation law. The delamination of interest here is the one in which the foulant layer de-adheres without arrest as analyzed in the analytical model; hence, the point of delamination is also determined through checking the contact area between the foulant layer and the film. Prior to delamination, the area remains almost flat. When the critical point is reached, the contact area drops rapidly signifying an unstable detachment at their interface.

*This simplifying assumption may not be realistic as G_{IIC} is often larger than G_{IC}, however, for computation simplification, such difference is neglected here(7).

Figure S3 shows typical stages in the compression process. When the nominal applied strain is smaller than the critical value for wrinkling to occur $\epsilon < \epsilon_w = \frac{1}{4}(3E_s/E_f)^{2/3} = 0.028$, the system remains flat (Figure S3a)(4, 8–14). Upon further compression above the critical value ϵ_w, the bilayer wrinkles. The foulant layer conformally follows this wrinkled topography (Figure S3b). When a critical amplitude A_c is reached, the foulant layer starts detaching from the bilayer surface (Figure S3c).

Utilizing this FE model with the prescribed CZM traction separation laws, we investigate the effect of σ_c and G on the onset of delamination. The mesh size is chosen such that at least 3-5 elements are inside the process zone length(15) $L_{pz} = E_p G/\sigma_c^2$. Note that for the right-triangular traction separation law used in the previous study for the elastic foulant layer(4), $G = 0.5\sigma_c^2/K$, this length becomes $L_{pz} = E_p/K$, where K is the initial stiffness of the traction law. Thus, the three parameters σ_c, K, and G are correlated in this implementation, making it difficult to separate the influence of individual parameters. However, the bi-linear profile offers an advantage to address this limitation. The initial stiffness K is set to a high value as required in CZM modeling and the influence of σ_c and G can be examined. Mesh sensitivity studies are conducted to show that similar results are obtained when the mesh size is refined. Furthermore, the effects of σ_c and G are also studied for several values of the foulant layer stiffness in order to connect the CZM approach and our analytical model. The following sets of material and geometric parameters are utilized for both solution approaches. The substrate thickness h_s is much bigger than the film thickness h_f so that the wrinkle pattern can be described as in the previous wrinkling work for bilayers(4, 8–14). The length of the system L is chosen so that it covers at least 8-10 wavelengths λ. The foulant layer thickness is selected to be in the thin layer limit(4) $h_p/\lambda < 1$, specifically here a ratio of $h_p/\lambda = 0.25$ is used unless otherwise stated. The materials properties for the substrate and film, and the instantaneous modulus $E_p(0)$ of the foulant layer are adopted from the previous study(4). The relaxation time τ_R and the amount of relaxation E_0/E_∞ are varied to study their influence on ϵ_c. The compression is applied as described in the work of Pocivavasek et al.(4). Specifically, for the elastic case, a displacement velocity that smoothly increased over 0.5 ms to the target $v_x = 0.01$ mm/ms was prescribed to the two ends of the tri-layer system with a loading rate $\dot{\epsilon}_{el} = 0.06$ ms^{-1}.

At the instantaneous and long-term response, the viscoelastic foulant layer can be treated as an elastic foulant layer with modulus E_p and the scaling law becomes(4): $\epsilon_c - \epsilon_w = a\lambda^2 G/B_p$. Using this scaling law, the normalized parameter $\widetilde{G} = \lambda^2 G/B_p$ will be utilized to analyze the FEM results. FE simulations of the delamination onset for the two cases, $\sigma_c/E_p = 0.15$ and $\sigma_c/E_p = 0.25$, with $E_p = 4.8$ kPa are shown in Figure S4. For each case, three states corresponding to $\widetilde{G} = 0.9, 1.8, 4.8$ are presented. As shown in the top three figures (Figure S4-a,b,c), at $\sigma_c/E_p = 0.15$, the first two cases (a,b) of $\widetilde{G}$ have almost the same critical delamination strain $\epsilon_c - \epsilon_w \sim 0.04, 0.05$, indicating that $\widetilde{G}$ does not play a significant role here. However, when $\widetilde{G}$ increases, it starts to take effect, i.e. $\epsilon_c - \epsilon_w \sim 0.12$ for the third case (Figure S4-c). The same trend is observed at $\sigma_c/E_p = 0.25$ where $\epsilon_c - \epsilon_w \sim 0.08, 0.08, 0.1$ in Figure S4-d,e,f, respectively. Furthermore, for the third value of $\widetilde{G}$, the two cases (Figure S4-c,f) have similar ϵ_c indicating that the change in the strength from $\sigma_c/E_p = 0.15$ to $\sigma_c/E_p = 0.25$ does not significantly influence ϵ_c.

These observations are consistent with the capacity of CZM to bridge different failure mechanisms as discussed in(16–18), but still requires further investigation in the context of our topography-driven delamination. As noted, the CZM process zone length, L_{pz} plays a key role in determining the transitions between these mechanisms(16–18). Figure S4 in the main manuscript plots the ratio $(\epsilon_c - \epsilon_w)/\widetilde{G}$ with respect to $L_{pz} = E_p G/\sigma_c^2$. The flat region is interpreted as the constant value for the slope of the linear scaling law between $\epsilon_c - \epsilon_w$ and $\widetilde{G}$. It indicates that σ_c is insensitive here and $\epsilon_c - \epsilon_w$ scales linearly with $\widetilde{G}_C$. However, if L_{pz} is too small or too large, σ_c might influence the results and deviate the solution from the energy based approach. Note that a pre-factor of approximately 0.025 is obtained from Figure 4 of the main manuscript. In order to compare this value with the one presented in the previous study for the case of elastic foulant layer (4), the correlation between amplitude and strain $A_c \sim \frac{\lambda}{\pi}\sqrt{\epsilon_c - \epsilon_w}$ can be used to determine the prefactor for the critical amplitude. This leads to a scaling: $A_c \sim 0.05\lambda^2(G/B_p)^{1/2}$ which is of the same order with the value $c = 0.13$ presented previously(4). They are not identical because, as discussed above, the right-triangular traction separation law has several numerical disadvantages and the effects of individual CZM parameters have not been investigated for this case as compared to the use of the bi-linear laws. However, the scaling dependence on $\widetilde{G}$ is consistent with analytical analysis with the same order of the numerical pre-factor for both cases of traction separation laws. In order to illustrate this region, Figure S5 plots the results from FEM for different cases of foulant layer's modulus and thickness. For each case, only the results of the sets of CZM parameters where σ_c has insignificant effect on ϵ_c are selected in this plot. The linear relationship observed in Figure S5 suggests that $\epsilon_c - \epsilon_w$ varies linearly with $\widetilde{G}$ as predicted by the scaling law.

Taking into account these considerations for CZM, we conducted FEM simulations with the viscoelastic foulant layer for L_{pz} in the energy dominated region $L_{pz}^- < L_{pz} < L_{pz}^+$. This allows a consistent comparison between FEM results and analytical model which focus on fracture driven by an energy release mechanisms. Results are presented in Figure S5 of the main manuscript.

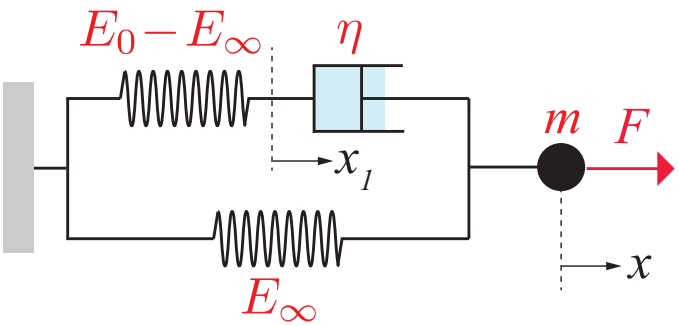

Fig. S1. A mechanical analog for a viscoelastic solid.

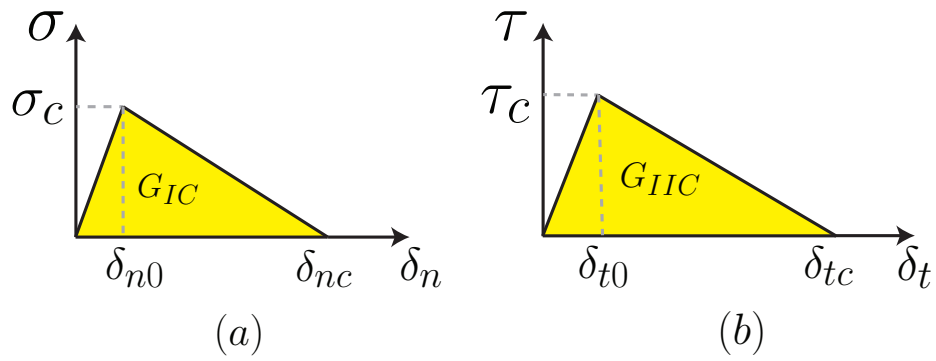

Fig. S2. Bi-linear traction separation laws for the normal and tangential modes. Delamination occurs when the tractions reach the ends of these traction laws and the separations attain the critical values δ_{nc} and δ_{tc} at which the energies G_{IC} and G_{IIC} are released to create the new surface.

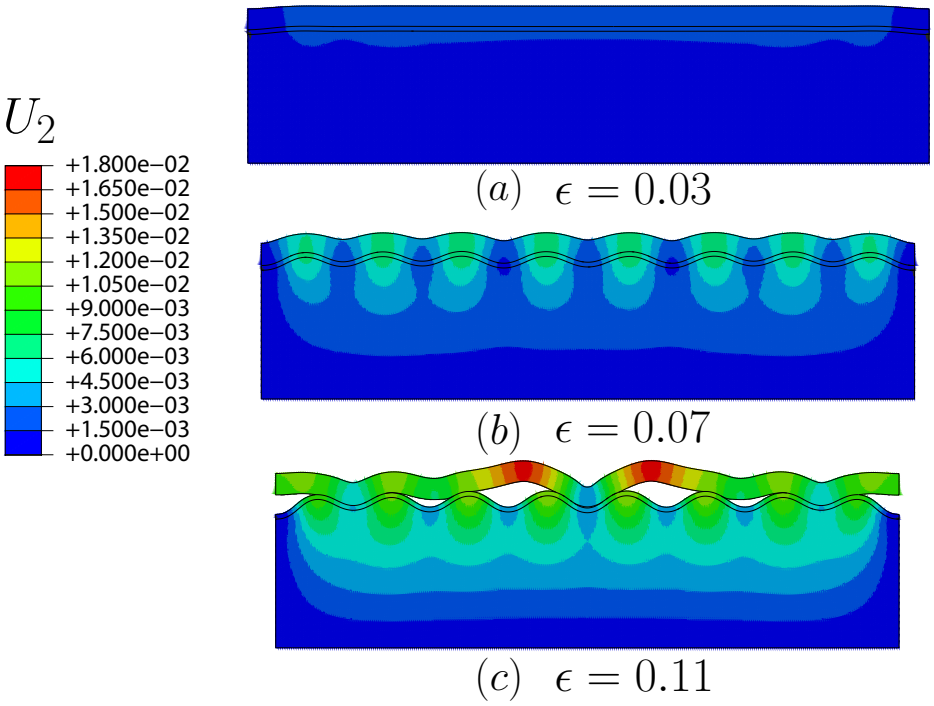

Fig. S3. Transitions from flat (a) to wrinkled (b) to delamination (c) stages in a typical FE simulation.

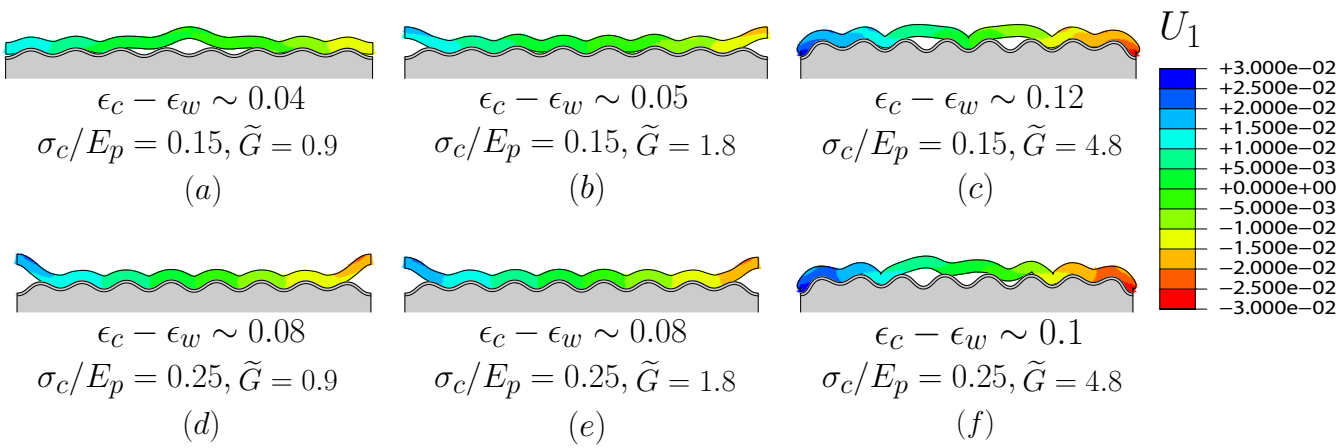

Fig. S4. FEM simulations showing critical delamination states in the foulant layer for two cases: $\sigma_c/E_p = 0.15$ (top) and $\sigma_c/E_p = 0.25$ (bottom). Three values of $\widetilde{G}_C$ are used: 0.9 (left), 1.8 (middle), 4.8 (right).

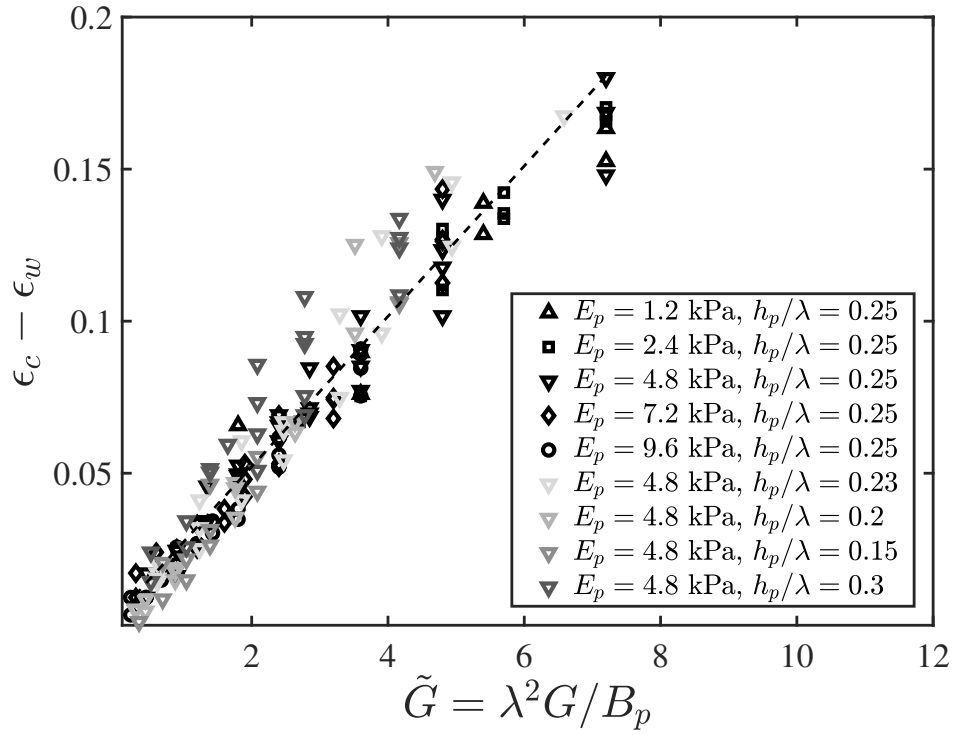

Fig. S5. $\epsilon_c - \epsilon_w$ with respect to $\widetilde{G}$ in the energy dominated regime. Various values of E_p and h_p are examined. The black dashed line is a fit showing the linear scaling as predicted from scaling analysis.

Movie S1. Thin, viscoelastic foulant layers follow the wrinkled topography and delaminate from the wrinkling surface when critical wrinkle amplitudes are reached. Compared to the slowly relaxing viscoelastic layer (left in the movie), the fast relaxing viscoelastic layer (right in the movie) is more difficult to detach.

References

1. RM Christensen, *Theory of Viscoelasticity.* (Dover Publications, New York), (2003).
2. H Chen, X Feng, Y Huang, Y Huang, JA Rogers, Experiments and viscoelastic analysis of peel test with patterned strips for application to transfer printing. *J. Mech. Phys. Solids* **61**, 1737–1752 (2013).
3. MV Srinivas, G Ravichandran, Interfacial crack propagation in a thin viscoelastic film bonded to an elastic substrate. *Int. J. Fract.* **65**, 31–47 (1994).
4. L Pocivavsek, et al., Topography-driven surface renewal. *Nat. Phys.* **3**, 948–953 (2018).
5. *Abaqus User's Manua* (Dassault Systèmes, MA, USA), (2018 [Online]).
6. JW Hutchinson, Z Suo, Mixed mode cracking in layered materials. *Adv. Appl. Mech.* **29**, 63–191 (1992).
7. N Nguyen, AM Waas, Continuum decohesive finite element modeling of fiber-reinforced polymer composites: mesh-objectivity and sensitivity studies in *58th AIAA/ASCE/AHS/ASC Structures, Structural Dynamics and Materials Conference, Grapevine, Texas.* (2017).
8. J Genzer, J Groenewold, Soft matter with hard skin: from skin wrinkles to templating and material characterization. *Soft Matter* **2**, 310–323 (2006).
9. HG Allen, *Analysis and Design of Structural Sandwich Panels.* (Pergamon Press, Oxford), (1969).
10. N Bowden, S Brittain, AG Evans, JW Hutchinson, WG M., Spontaneous formation of ordered structures in thin films of metals supported on an elastomeric polymer. *Nature* **393**, 146–149 (1998).
11. L Pocivavsek, et al., Stress and fold localization in thin elastic membranes. *Science* **320**, 912–916 (2008).
12. J Sun, S Xia, M Moon, KH Oh, K Kim, Folding wrinkles of a thin stiff layer on a soft substrate. *Proc. R. Soc. A* **468**, 932–953 (2012).
13. Y Cao, JW Hutchinson, Wrinkling phenomena in neo-hookean film/substrate bilayer. *J. Appl. Mech.* **79**, 031019 (2012).
14. C E., L Mahadevan, Geometry and physics of wrinkling. *Phys. Rev. Lett.* **90**, 074302 (2003).
15. A Turon, CG Davila, PP Camanho, J Costa, An engineering solution for mesh size effects in the simulation of delamination using cohesive zone models. *Eng. Fract. Mech.* **74**, 1665–1682 (2007).
16. K Golovin, A Dhyani, MD Thouless, A Tuteja, Low–interfacial toughness materials for effective large-scale deicing. *Science* **364**, 371–375 (2019).
17. JP Parmigiani, MD Thouless, The effects of cohesive strength and toughness on mixed-mode delamination of beam-like geometries. *Eng. Fract. Mech.* **74**, 2675–2699 (2007).
18. C Heinrich, AM Waas, Investigation of progressive damage and fracture in laminated composites using the smeared crack approach in *53rd AIAA/ASME/ASCE/AHS/ASC Structures, Structural Dynamics and Materials Conference, Honolulu, Hawaii.* (2012).